Evolution of galaxy dynamics over the last 10 Gyrs with MUSE/VLT

Master Thesis

Author: Mercier Wilfried
Supervisor: Contini Thierry
Co-Supervisor: Epinat Benoît

Observatoire de Paris
Institut de Recherche en Astronomie et Planétologie

May 20, 2019

Abstract

Contents

List of Figures

List of Tables

1 Introduction

1.1 Photometry and spectroscopy in galactic astronomy

1.1.1 Photometric data

Photometric and spectroscopic data have been widely used in the past to study questions related to the formation and evolution of galaxies at both low and high redshifts. Photometry is a key component in the study of galaxy light profiles and the location of the different stellar populations.

Assuming the galaxies are resolved enough within the images, photometry gives us information about their morphological properties and can tell us how their content is distributed within them. Observations in different wavelength ranges (bands) give us insight into the differences in distribution between young and old stars (observed respectively in UV and near IR rest-frame bands), which can in turn indicate the presence of HII regions[1] (citation here). Typical wavelengths of observation include the visible spectrum, IR and UV. Ground based near-IR (NIR) photometry can also give information on the distribution of gas and old stars, and space based telescopes observing in the far-IR (FIR) can give us insight into the location of dust. Being able to determine the amount of dust along the line of sight, the so called column density defined as the 3D density integrated along the line of sight, is most important as it is mandatory to derive any robust estimates of absolute magnitude and Star Formation Rate (SFR).

Photometric information of galaxies is generally obtained through model fitting of the measured light profile, though other methods exist involving growth of ellipses (cite here).

The most commonly used model of galaxy shape, excluding more complicated cases such as irregular structures and merging galaxies, is a Sérsic profile which we generally write as (Graham et al., 2005)[2]

$$I(r) = I_{\mathrm{e}} e^{-b_n\left(\left(\frac{r}{R_{\mathrm{e}}}\right)^{1/n}-1\right)} \tag{1}$$

where r is the radial distance to the morphological centre of the galaxy, n is referred as the Sérsic index of the galaxy, R_e is the effective radius (also called half-light radius) which encloses 50% of the total luminosity of the galaxy, I_e is the intensity at the position R_e and b_n is a term which ensures that R_e does enclose half the total luminosity. The formal definition of b_n can be shown to be such that $2\gamma(2n, b_n) = \Gamma(2n)$ with γ and Γ respectively the incomplete and complete gamma functions.

This equation can simplify into two famous galaxy profiles:

[1] Clumpy regions of ionised hydrogen with high values of star formation.

[2] The original definition $I(r) \propto e^{(r/\alpha)^{1/n}}$ from Sérsic (1963) was modified to Eq. 1 because of the too small (immeasurable) values α generally takes.

- an exponential disc for $n = 1$ which represents a disk-like/spiral[3] galaxies
- a de Vaucouleurs profile for $n = 4$ which describes elliptical (early-type) galaxies

This model with a freely varying Sérsic index is the one used in some morphology fitting software such as SExtractor (Bertin & Arnouts, 1996) or GIMD2D (Simard, 1998), but other forms can also be used from time to time. For instance one can use a combination of a bulge and a disk, with two fixed Sérsic indices instead of one allowed to freely vary, as in GALFIT (Peng et al., 2002).

Morphological parameters derived from the morphology modelling can then be used in various ways. We can classify the galaxies as elliptical or spiral using their Sérsic index or the most dominant feature between the disk and the bulge component if the modelling was a combination of both. We can also derive a value for the inclination of the galaxy on the sky using the ratio between the minor and major axes. Indeed, if we define the inclination of a galaxy as the angle between the normal to its plane and our line of sight, we have the relation

$$\cos i = b/a \tag{2}$$

where b is the galaxy minor axis and a its major axis.

If many photometric observations have been carried out on the same sky patch in multiple bands as in the case in the COSMOS field (see Section), different stellar populations and gas components can be observed. This gives us an approximate spectrum from which we can derive, for instance, a more precise photometric redshift than by combining a single instrument with multiple filters (insert citation here) and allows one to perform an SED fitting on this spectrum to derive other useful estimates such as the stellar mass, mean metalliticity or star formation rate (citation here).

From both SED fitting and morphological parameters, it is then possible to derive scaling relations between them. For instance, we can derive the Tully-Fisher relation for late-type galaxies which relates the total luminosity of the galaxy with its maximum rotational velocity, or the Faber-Jackson relation for early-type galaxies where we use the velocity dispersion instead of the maximum rotational velocity (citation here).

The main drawback for having multiple band photometry is that it requires long observation times of the same sky area with different telescopes probing different wavelength ranges. Thus, it is not well suited to the study of galaxies' spectral features and therefore their kinematics.

[3]We will preferentially use the terms disk-like/late-type galaxies, with respect the Hubble sequence (Hubble, 1922), (Hubble, 1926), rather than spiral galaxies since many of the galaxies studied in the present work do show a disk morphology without clear spiral arm patterns.

1.1.2 Spectroscopy

On the other hand, astronomers have also been using spectroscopy to study galaxy chemistry, gas abundance and its kinematics. Contrary to photometry, these methods of observation do not yield an image of the galaxy but instead a spectrum of the pointed area. From such spectra, assuming we are able to unambiguously detect a spectral feature such as a ray (Hα, Hβ, OII, OIII, Lyα, etc.) or a line break (generally Lyman or Balmer break), we can infer a much more precise value for the galaxy redshift than in the photometry case as well as the gas velocity and its dispersion.

The lack of imaging implied that these methods only returned overall information on the whole galaxies or in specific regions chosen in advance for their scientific interest (HII region for instance). This was the case until slit spectroscopy was developed. Opposite to what has been previously said, slit spectroscopy give spectroscopic information not in a single pixel, but along a slit. Galaxies studied with this method generally relied on prior morphological information

Such data gives us information about how the gas moves inside the galaxies and allows one to classify the galaxies based on their kinematics (rotationally supported or dispersion dominated, see insert citation here).

In this context, it has become clear that a combination of these techniques would be necessary to better constrain the models of galaxy formation and to study in more details the origin of the observed scaling laws (SFR-mass, mass-size, luminosity-mass relations, etc.). In recent years, this has become possible with the advent of Integral Field Spectroscopy (IFS) astronomy. This technique combines the advantages of both photometry and spectroscopy by measuring the spectrum of each pixel in an image, yielding a 3D cube with two spatial and one spectral dimensions. Such instruments lacked for the most part a good spatial resolution until recently, but have now filled the gap.

1.2 MUSE-VLT

MUSE is an Integral Field Unit (IFU) mounted on the VLT in Chile which spans a $1' \times 1'$ Field of View (FoV). Its wavelength range covers both the visual spectrum and the Near Infra-Red part (NIR), going from 4650 Å to 9300 Å. This instrument was built with the main purpose of performing blind searches of sources in the field. The wavelength range is well suited to detect the OII doublet in the redshift range 0.4, 1.4.

2 Sample selection

2.1 COSMOS field

Group ID[1]	Ra[2] J2000 (°)	Dec[3] J2000 (°)	Exposure[4] (hr)	Average seeing[5] (")	Total nb. galaxies[6]	Nb. field galaxies[7]
CGr32	NaN	NaN	3×4.35	0.51 - 0.58	NaN	NaN
CGr34_d	149.87766	2.502331	5.25	0.63	NaN	NaN
CGr34_bs	149.87766	2.502331	4.75	NaN	NaN	NaN
CGr30_d	150.144225	2.065971	9.75	0.67	NaN	NaN
CGr30_bs	150.144225	2.065971	6.25	NaN	NaN	NaN
CGr84	150.057219	2.599744	5.25	0.59	NaN	NaN
CGr84-N	NaN	NaN	1	0.51	NaN	NaN
CGr114	149.994285	2.258044	2.2	0.68	NaN	NaN
CGr79	149.820686	1.821825	4.35	0.60	NaN	NaN
CGr28	150.218094	1.812667	1	0.62	NaN	NaN
CGr26	150.492767	2.069139	1	0.59	NaN	NaN
CGr61	149.728741	1.915987	1	0.64	NaN	NaN
CGr51	149.982756	1.801899	1	$0.6 - 0.7$	NaN	NaN
CGr23	149.790782	2.162648	1	0.68	NaN	NaN

Table 1: Main characteristics of the observed MUSE fields. Groups ending with _d correspond to deep observations (full stacked OBs) and with _bs correspond to best-seeing observations (only OBs with a seeing below 0.7"). The seeing is given for the OII wavelength at the group's redshift. 1. MUSE group number, 2. Group centre's right ascension, 3. Group centre's declination, 4. Duration of observations, 5. Average seeing during observation, 6. Total number of detected galaxies within MUSE FoV, 7. Number of field galaxies found by the FoF algorithm.

The point of the analysis is to perform a joint study of the morphology and the kinematics of field galaxies in the COSMOS field using respectively HST ACS images and MUSE data. To this end, a set of 9 galaxy groups in the COSMOS field was selected. The choice of the COSMOS field for this analysis was made because of the large number of multi-band photometric data available for the galaxies in this field and the presence of rich (large number of member galaxies) galaxy groups.

Guaranteed Time Observations (GTO) centred on the groups were performed from which 13 different MUSE Fields of View (FoV) of $1 \times 1\,\mathrm{arcsec}^2$ were obtained. Each FoV is composed of many Observation Blocks (OB) of 30 min each with the Position Angle (PA) of the instrument rotated by 90° between consecutive OBs.

Most of the groups correspond to one FoV, except for CGr32. Since this group is larger than the others, three slightly overlapping FoVs were taken around it. A a couple of groups were also split into *deep* and *best-seeing* observations, the former combining all the OBs into one FoV regardless of the average seeing in each OB, when the latter only

kept OBs with an average seeing larger than 0.7".

The main characteristics of the observed FoVs, including the position of their centre, the exposure per FoV, the average seeing during the observation, the total number of galaxies and the number of field galaxies detected by the FoF algorithm are listed in Table 1.

These groups were primarily chosen for their position within the COSMOS field. This ensured them to have a large set of corresponding photometric data available from Laigle et al. (2016) catalogue for most of the galaxies. Nevertheless, since blind source detections within the data cubes were performed on these FoVs, we also had a small fraction of galaxies which were detected in MUSE cubes but not in the HST images.

Indeed, galaxies detected by MUSE were for the most part also detected in HST images because the HST much better resolution (0.03 arcsec/px for HST and ~ 0.2 arcsec/px for MUSE). Nevertheless, the blind source detection algorithm (insert name and citation here) used in the MUSE pipeline is able to detect additional sources in regions where there is no HST counterpart by differentiating spectral features, even though the sources are blended below the MUSE PSF (?, ?).

2.2 Prior information on the galaxies

2.2.1 Cluster galaxies

This internship was planned to be similar in many aspects to what has been doing Epinat B. PhD student Valentina Abridg in LAM, Marseille for her PhD. Her work consisted in studying the morphology and the kinematics of the galaxies within the structures observed by MUSE in the COSMOS field. The galaxies she studied were therefore found in the same FoVs as those we are using in this work, but belonged to groups instead of being labelled as field galaxies.

To differentiate between group and field galaxies, a Friend of Friends algorithm (FoF) was run prior to my arrival on the galaxies in each FoV. Thus, each galaxy was labelled either as belonging to a group (potentially more than one per FoV) or as field galaxies.

Additionnaly, a morphological analysis had already been performed by Valentina with GALFIT only on cluster galaxies. Two Sérsic profiles with fixed Sérsic indices ($n = 1, 4$) were used to describe the cluster galaxies as a combination of a disk and a bulge component. Hence, the intensity of the modelled galaxies can be written as

$$I(r) = I_{e,\mathrm{d}}\, e^{-b_1\left[\frac{r}{R_\mathrm{d}}-1\right]} + I_{e,\mathrm{b}} e^{-b_4\left[\left(\frac{r}{R_\mathrm{b}}\right)^{1/4}-1\right]} \tag{3}$$

where $I_{e,\mathrm{d}}$, $I_{e,\mathrm{b}}$ are the effective intensities of respectively the disk and the bulge component and R_d, R_b their respective half-light radii.

Therefore, we already had morphological information for roughly half of the total sample including model parameters as described above, but also morphological parameters such as the ellipticity of the galaxies, the Position Angle (PA) of their kinematical main axis (which can be different from the morphological PA).

2.2.2 Morphological information from COSMOS catalogues

The total number of galaxies detected by MUSE in the COSMOS field is around 1000. Roughly half of them belong to clusters and the other half are labelled as field galaxies. Among these galaxies, not all of them are useful to our study. Some may be too close to the edge of detection, others be too noisy with a low Signal to Noise Ratio (SNR), or too small to perform any relevant kinematical modelling. It is thus mandatory to apply a selection on our data set of field galaxies, first to save time for the analysis, but also to reduce uncertainties.

Our goal is to perform a joint study of the morphology and the kinematics of these galaxies. The tools and the models for the kinematical modelling were already developed as they were used by Valentina for her PhD. On the other hand, fitting morphological models with software such as GalFit or SExtractor would have required additional time which we did not have. Hopefully for us, morphological modelling had already been performed on the galaxies in the COSMOS field, so we could focus on the kinematical part.

Morphological information for all the galaxies in the COSMOS field can be found in various catalogues and tables[4]. To start with, we decided to use the two most complete catalogues we could find, that of Tasca (maybe citation) and Cassata (maybe citation as well). Both catalogues contain morphological information including the central position of the galaxy, its half-light radius, concentration and asymmetry parameters, ellipticity, Position Angle of the major morphological axis (PA), and many more for roughly 232000 galaxies. The authors obtained the morphological information by running SExtractor on HST images of the galaxies in the COSMOS field given in Laigle et al. (2016) catalogue.

Since we already had a table containing information for our galaxies from the MUSE pipeline and also from Laigle et al. (2016) catalogue, we only had to cross-match our table with Cassata's and Tasca's catalogues to collect the morphological information of the galaxies. We decided to cross-match our data with each catalogue separately and then with both using the right ascension α and declination δ of the centre of the galaxies, allowing for a maximum separation between the MUSE source and the closest source within Cassata's and Tasca's catalogues of 1 arcsec maximum.

This cross-matching procedure was performed for both field and cluster galaxies. The

[4] `https://irsa.ipac.caltech.edu/data/COSMOS/tables/morphology/`

reason for cross-matching cluster galaxies when we are only interested in those in the field will be discussed in the following section.

2.3 Checking catalogues values consistency

2.3.1 Reasons for checking catalogues values

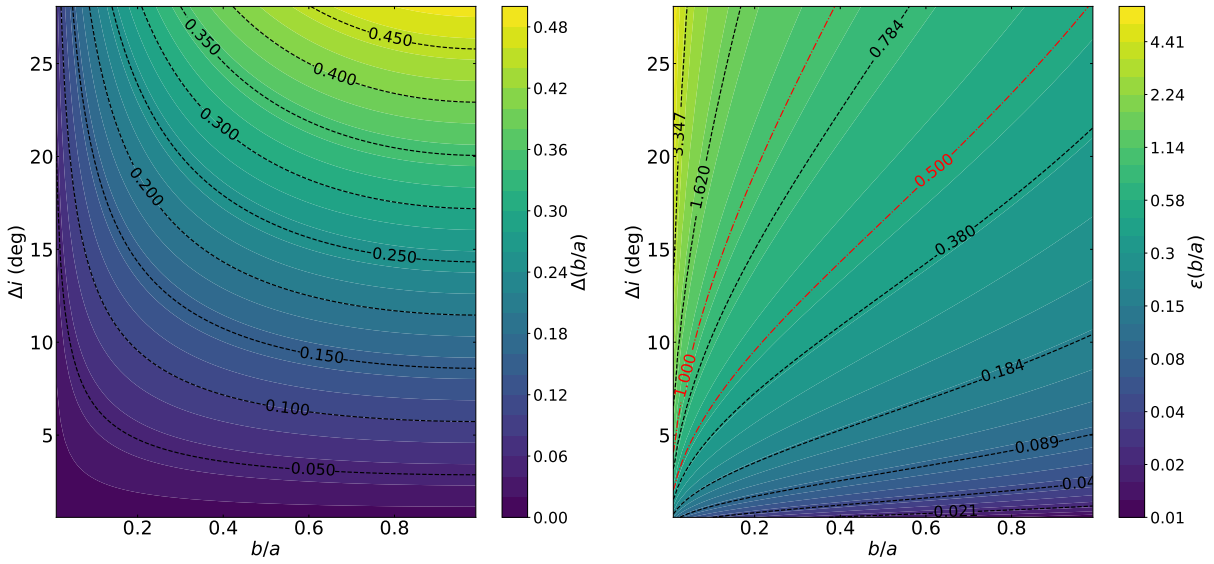

(a) Error on inclination as a function of b/a and its absolute error. Contours of $\Delta(b/a)$ are plotted in black dashed lines with their corresponding value.

(b) Error on inclination as a function of b/a and its relative error. Contours of $\epsilon(b/a)$ are plotted in black and red dashed lines with their corresponding value.

Figure 1: Error on inclination as a function of b/a and its error. Left: as a function of the absolute error on b/a ($\Delta(b/a)$). Right: as a function of the relative error on b/a ($\epsilon(b/a)$). Red contours correspond to values for which there is a 50% and 100% error on b/a.

As in any analysis, we must select a sample based on relevant criteria in order to remove uninteresting data. This selection can only be done by comparing morphological parameters values and overall spectral features since any kinematical modelling relies on prior morphological information.

Before this internship, spectral fitting on the integrated spectra of the galaxies had already been done, and we knew we already had morphological information from COSMOS catalogues as discussed in the previous section. Potentially useful morphological information included half-light radii, magnitudes, ratios of minor to major axis (b/a) or equivalently a measure of the ellipticity of the galaxies.

Nevertheless, using this data without checking first how well it compares to values found in other catalogues and/or derived using different softwares/models could lead to high biases and uncontrolled errors. Thus, before discussing any selection criteria for our sample, we must first assess the reliability of the parameters we are going to use in later

sections.

The three most important values for us are the half-light radius, as it will be used to select our sample, the total magnitude and the b/a ratio. The last parameter has a crucial importance since it is directly related to the inclination of the galaxy on the sky through Eq. 2. Given a certain error $\Delta(b/a)$ on the axes ratio, and using the usual formula for computing the error $\Delta f = |\partial_x f|\Delta x$ of a function $f(x)$, we find for the inclination

$$\Delta i = \Delta(b/a) \left| \frac{b}{a}\left(2 - \frac{b}{a}\right)\right|^{-1/2} \tag{4}$$

This is illustrated in Fig. 1 where Δi has been plotted as a function of b/a and its error (absolute on the left, relative on the right). Contours of the error on b/a have been over-plotted to show how evolves Δi given a fixed error on b/a. As expected, the higher the error on b/a the higher the error on i. An error as high as 50% could yield $\Delta i \approx 27°$, though this value is reached for $b/a \approx 1$ where the axes ratio is the least constrained by the morphology. A more appropriate error on b/a of 20% gives a maximum Δi slightly above 10°, which is correct.

Since the inclination has an impact on the maximum rotational velocity, and so potentially on the classification of galaxies as rotationnaly supported or dispersion dominated (see Section insert ref here), this indicates us that for any proper kinematical modelling we must check carefully that the values of axes ratios are consistent between catalogues.

2.3.2 Catalogues used for comparison

As stated in previous sections, we cross-matched our catalogue of galaxies detected by MUSE in the COSMOS field with Cassata's and Tasca's, two tables with morphological information for the galaxies found in Laigle et al. (2016).

However, as this will be showed in the following sections, it turned out that there were large discrepancies between the parameters we studied. Thus, to better understand the origin of these discrepancies, we chose to cross-match a last time our catalogue with another one (also based on Laigle et al. (2016)) from Zurich. This table has fewer HST counterparts of MUSE galaxies than in the other two but it contains additional morphological information which we can use for the comparison.

In addition to that, we already had morphological information from GALFIT fits on $\sim$ 500 group galaxies, and we had strong confidence in the given morphological values. Therefore, we chose to compare the data in the three morphological catalogues based on Laigle et al. (2016) with that of GALFIT.

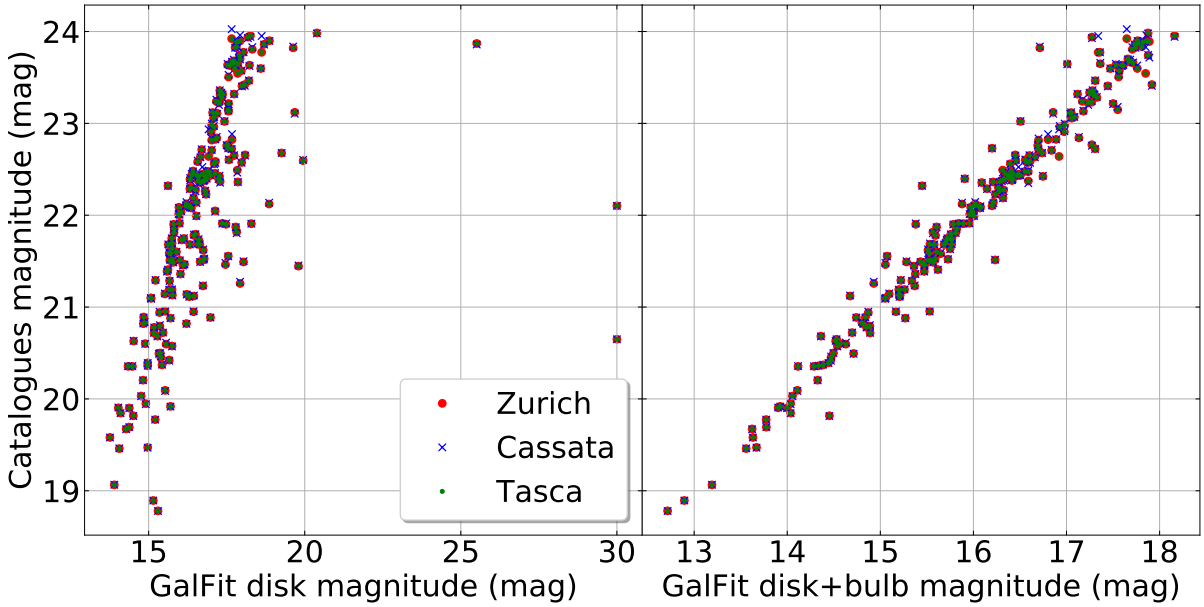

Figure 2: Comparison between the morphological catalogues magnitudes and that of GALFIT for cluster galaxies. Magnitudes from the catalogues agree well between each other. Left: compared with GALFIT disk magnitude only. The slope is too high and a few points are scattered far from the line. Right: compared with the total GALFIT magnitude as defined in Eq. 7. We find a good linear relation with poor scatter.

2.3.3 Comparing total magnitudes

The first value we can easily compare is the magnitude. Cassata's, Tasca's and Zurich's catalogues provide a measure of the total magnitude derived from fitting with SExtractor a single Sérsic profile with a free Sérsic index n on HST images.

Since GALFIT had been run on the group galaxies by fitting two Sérsic profiles with fixed Sérsic indices ($n = 1, 4$), we had two measures of the magnitude of these galaxies: one for the bulge component $m_{\rm b}^{\rm GF}$, and another for the disk component $m_{\rm d}^{\rm GF}$. To have a meaningful comparison between magnitudes, we need to compute the GALFIT total magnitude by combining the bulge and the disk components. Both are defined as

$$m_i^{GF} = -2.5 \log_{10} \left(F_i^{\rm GF} \right) + {\rm C} \tag{5}$$

where $i = {\rm b}, {\rm d}$ represents either the bulge or the disk, $F = L/4\pi D^2$ is the flux of the galaxy in some band, L its intrinsic luminosity, D its cosmological luminosity distance to us and C a constant depending on the band used.

Considering that the two components have different luminosities but are located at the same distance, we can add the fluxes together. Thus the total GALFIT luminosity can also be written as

$$m_{\rm tot}^{\rm GF} = -2.5 \log_{10} \left(F_{\rm b}^{\rm GF} + F_{\rm d}^{\rm GF} \right) + {\rm C} \tag{6}$$

Inverting Eq. 5 to get the components flux as a function of their magnitude and inserting it into Eq. 6 yields

$$m_{\rm tot}^{\rm GF} = -2.5\log_{10}\left[10^{-\frac{m_{\rm b}}{2.5}} + 10^{-\frac{m_{\rm d}}{2.5}}\right] \tag{7}$$

This is the value that should be compared with the three catalogues magnitudes. Fig. 2 shows how these scale with each other and with GALFIT disk magnitude on the left, and the total magnitude from Eq. 7 on the right. As expected, the catalogues give the same value except for a few points. We see that the total GALFIT magnitude gives a much better, poorly scattered linear relation with the catalogues magnitudes. Even though there is an offset between GALFIT and the catalogues, this is due to using different conventions for the constant term in Eq. 5.

We reached the same conclusion for field galaxies as well. Thus, we find a good agreement between our values and that of GALFIT.

2.3.4 Morphological type classification

We might expect to have some discrepancies in our data because of the models used between GALFIT and SExtractor/GIM2D. A way to check this effect is to study how these differences scale with the morphological type of the galaxies. For instance, if we use the disk half-light radius of GALFIT to compare with that of SExtractor, we might expect to have some scatter in our relation for the elliptical galaxies as the disk component is not the best one to describe them.

To see how these relations scale with morphological types, we can use the classification given in the three morphological catalogues:

- Cassata's catalogue gives a classification based on morphological parameters they derived with SExtractor. To do so, they use a reference of 500 galaxies with known parameters which they visually classify as either elliptical, disk-like/spiral or irregular. From this set, each time a new galaxy must be classified, its 11 closest neighbours are inspected and the most frequent class is assigned to the galaxy.

- Tasca's catalogue gives different classifications based on three methods. The first one is similar to the one used by Cassata. This is also the classification they recommend to use because this is the one they put the more their trust in. The second one uses the technique described in (insert Abraham 1996 here) using the asymmetry and concentration parameters. The last one uses a support vector machine to classify galaxies.

- Zurich's catalogue gives a single classification named Zurich Estimator of Structural Type (ZEST) described in (insert Scarlata, Carollo, Lilly et al 2007, ApJS, 172,

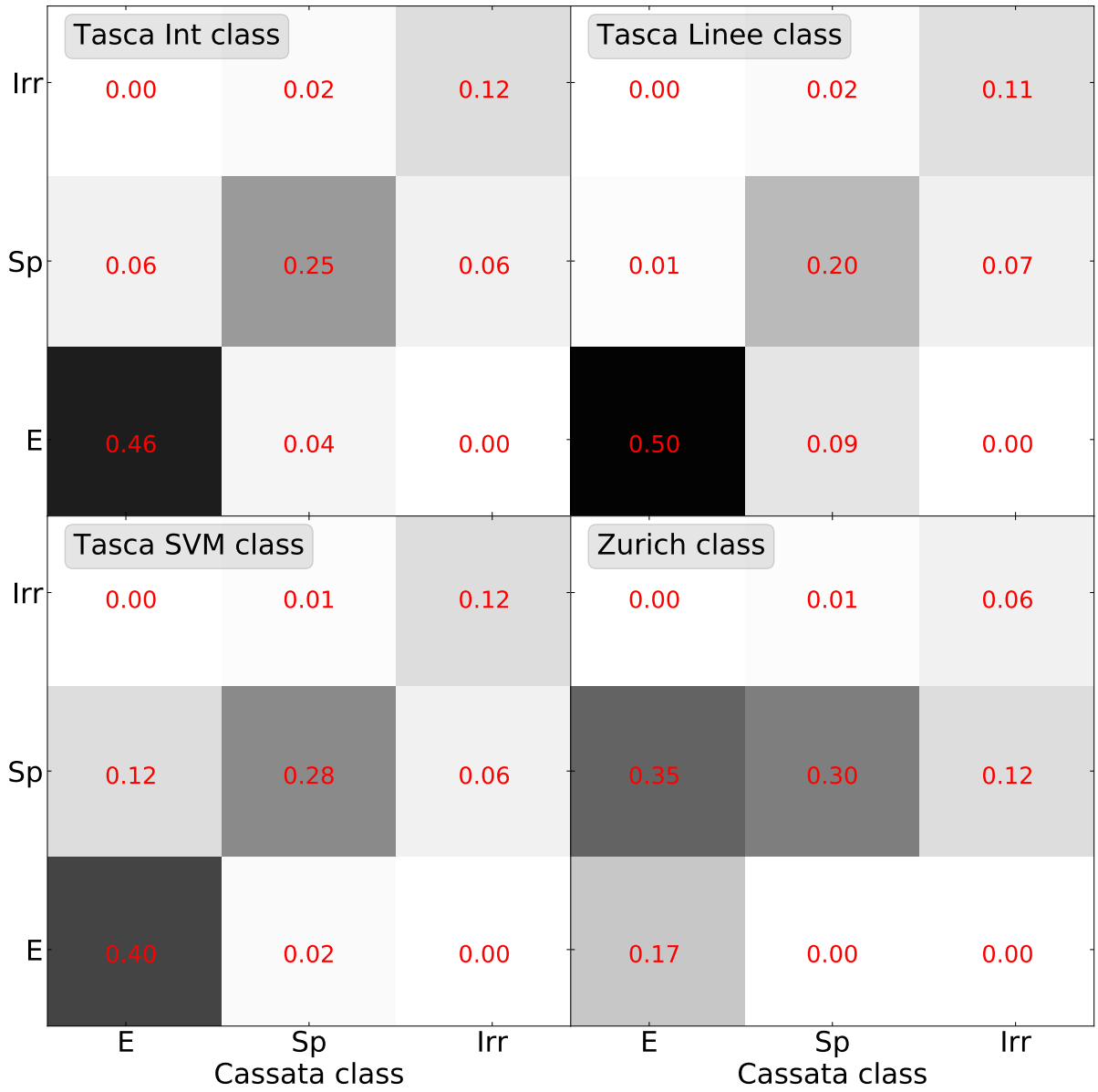

Figure 3: Comparison between morphological types given in Tasca and Zurich catalogues against that of Cassata. The three classifications of Tasca are those described in Section 2.3.4. Galaxies are labelled as follows: E for ellipticals, Sp for spirals/disks-like, Irr for irregulars. We find good agreement between Tasca and Cassata types but not between Cassata and Zurich.

406)

2.3.5 Comparing half-light radii

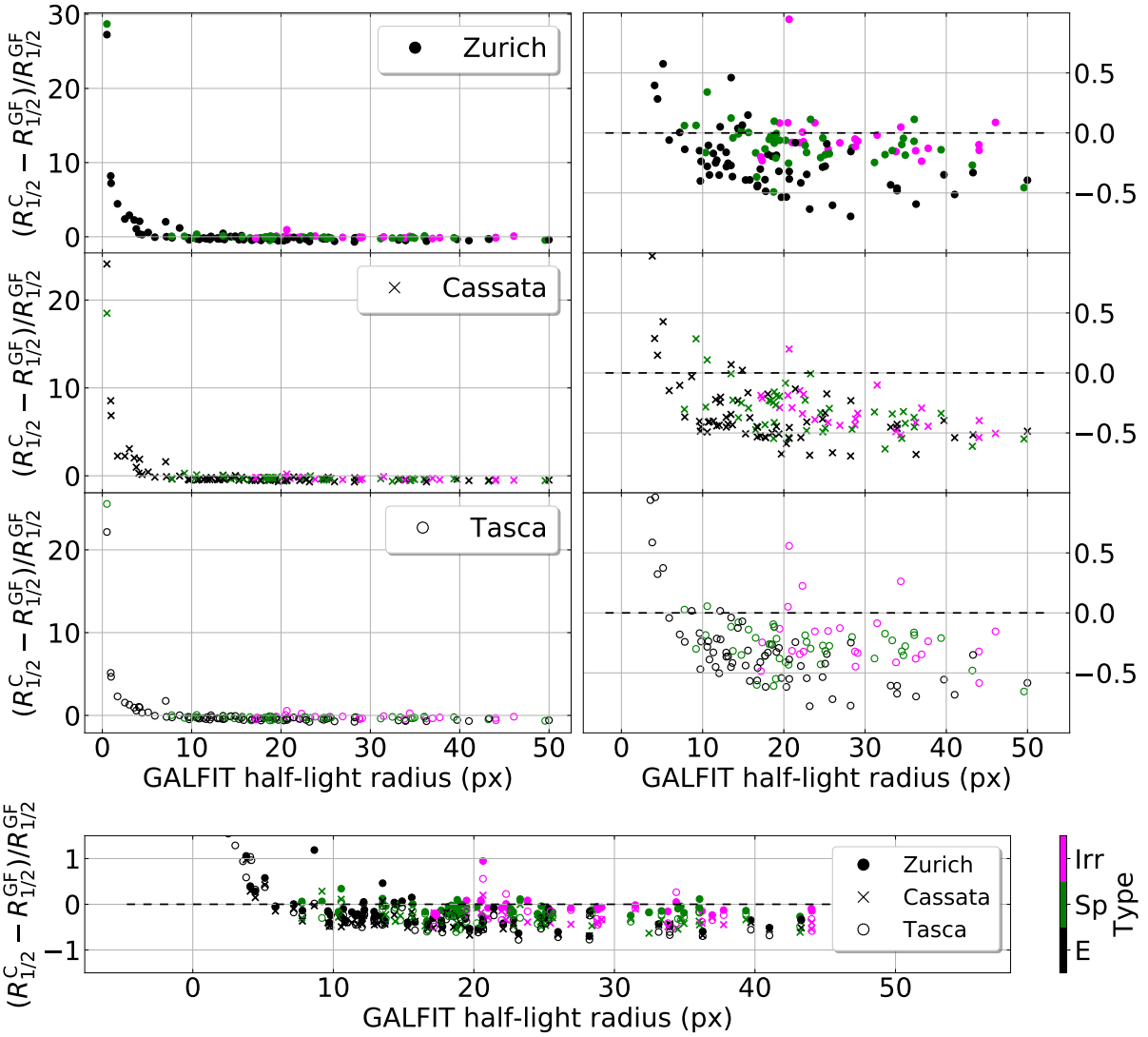

Figure 4: Comparison between half-light radii from the morphological catalogues and the radius of GALFIT disk component. The relative error is shown for the three catalogues (from top to bottom, Zurich, Cassata and Tasca). Points have been colour coded according to their classification given in Cassata's catalogue (Irr for irregular, Sp for spiral/disk, E for ellipticals). Left: the full range is plotted. Right: a zoom on the points with $R^{GF}_{1/2} \geq 5\,\mathrm{px}$. The last plot on the bottom combines the information within the three plots on the left.

One of the most important parameters we have to check before the selection is the half-light radius of our galaxies. Indeed, if we underestimate it, we might remove from our sample resolved galaxies and therefore reduce our statistics. On the other hand, overestimating it would give us too many unresolved galaxies for which we would spend time performing the cleaning routine without being able to perform their kinematical analysis in the end.

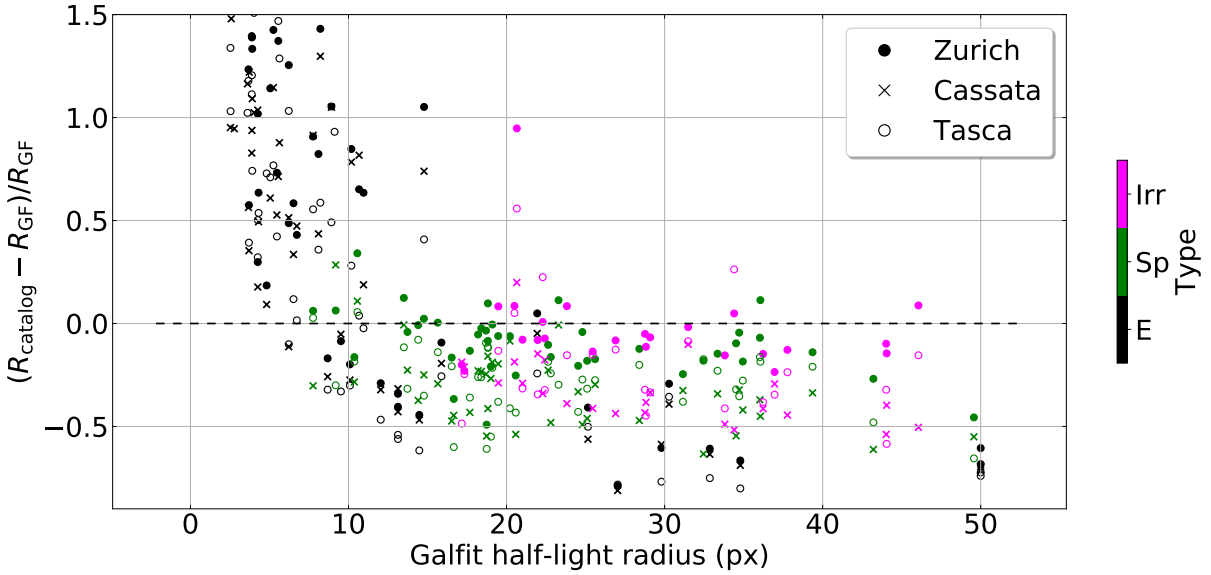

Figure 5: Comparison between catalogues radii and that of GALFIT. This figure is similar to Fig. 4 but GALFIT radius for elliptical galaxies is that of the bulb instead of the disk. The catalogues appear to overestimate the elliptical galaxies radii when using GALFIT bulge radius.

Hence, it is mandatory to thoroughly check the values of the half-light radius from the three catalogues against that of GALFIT, and understand the origin of any discrepancies if there happens to be some.

It turns out that we discovered a quite large disagreement between GALFIT radius and the values given in the catalogues, and even among them. This is illustrated in Fig. 4 where the half-light radii are compared against that of GALFIT. Galaxies are colour coded according to the classification given in Cassata's catalogue. We checked that using Tasca's three classifications as described in Sec. 2.3.4 did not change our conclusions. In these plots, we decided to use for the x-axis the half-light radius of GALFIT disk component for all the galaxies, even though we might expect the elliptical galaxies to be better described by their GALFIT bulge half-light radius.

We observe large differences in radius for low $R^{\mathrm{GF}}_{1/2,d}$, but this is expected. Indeed, catalogues half-light radii are computed using SExtractor which does not take into account the PSF in its fit, contrary to GALFIT. Thus, it makes sense to have an overestimation of the radius in these catalogues when reaching low values of $R^{\mathrm{GF}}_{1/2,d}$.

On the other hand, when we focus on galaxies with a GALFIT radius larger than $\sim 5\,\mathrm{px}$, we observe a global underestimation for all the catalogues, up to roughly 50%. This scatter comes from elliptical galaxies. On the contrary, radii of disk-like galaxies have the least scatter and biais, especially those given in Zurich's catalogue. This is also something we might have expected since, as mentioned above, the GALFIT disk half-light radius might not be the best parameter to use for comparing elliptical galaxies.

If we decide to split the galaxies into two categories, ellipticals and disks/irregulars, and if we use for the first category $R^{\rm GF}_{1/2,b}$, and for the second $R^{\rm GF}_{1/2,d}$ we find that elliptical galaxies half-light radii in the catalogues are now overestimated as shown in Fig. 5. This result, and the underestimated values when using the disk radius for the elliptical galaxies, indicates us that elliptical galaxies seem to be neither dominated (in terms of radius) by the disk component, nor by the bulge in the GALFIT model. It is thus necessary to directly compute an overall half-light radius by integrating the galaxies light profile given in Eq. 3

2.4 SNR and size selection criteria

2.4.1 Size selection

Since we are interested in keeping well resolved field galaxies, we need to apply relevant criteria in order to select the right galaxies. The most obvious parameter we can use to make our selection is the size of the galaxy, though we must be certain before using it that the value given in our cross-matched catalogue reflects accurately enough the "true" size of the galaxy. This checking is performed and discussed in the next section.

Following the earlier work done in Bacon et al. (2015) and Bacon et al. (2017), the MUSE Point Spread Function (PSF), that is the pattern we obtain when we observe a point-like source with MUSE, is most well described by a Moffat (1969) profile

$$I_{\rm PSF}(r) = I_0(1 + (r/\alpha)^2)^{-\beta} \tag{8}$$

where r is the radial distance to the centre and α, β are two seeing dependant parameters. In our case we are interested in the Full Width at Half Maximum (FWHM) since it is directly related to the seeing conditions and it gives us information about the minimum spatial extent within which data will be mixed up. The FWHM can be easily derived from the equation $I_{\rm PSF}({\rm FWHM}/2) = {\rm I}_0/2$, from which we get the following relation

$${\rm FWHM} = 2\alpha\sqrt{2^{1/\beta} - 1} \tag{9}$$

According to the aforementioned articles the value of β should remain roughly constant and we would expect from differential image motion theory (insert this paper here when read 10.1086/342683) that the FWHM would linearly decrease with wavelength. Thus, if we want to derive the FWHM at a given wavelength and in a given field (since the seeing conditions will vary with the date of observation) we need to derive the linear relation between the FWHM and the wavelength in each field.

The measure of α, and therefore the FWHM, was obtained by Valentina on at least two stars by FoV. Because they belong to our galaxy, we can consider that they have a

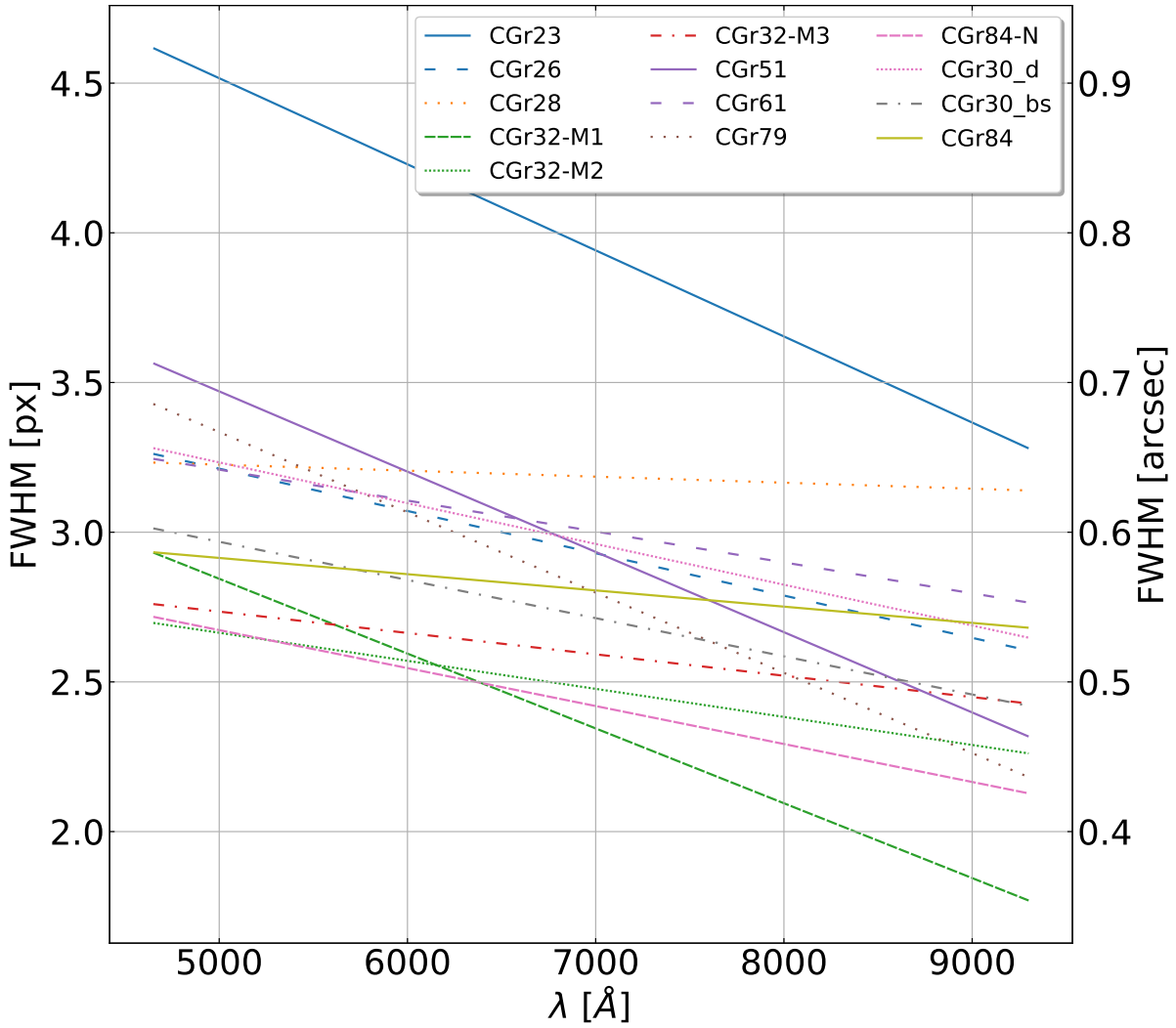

Figure 6: PSF FWHM variation with wavelength for the 13 FoVs as measured by Valentina. At least two values of the FWHM were derived from stars in the FoVs by fitting a Moffat distribution to their light profile. We assumed a linear evolution with wavelength. Strong fluctuations appear depending on the observed FoV.

null redshift, so that the wavelength of observation and emission are the same.

A Moffat profile was fitted on their OII λ3727 Å and OIII 5007 Å flux maps, giving us at least two measures of the FWHM . Though a more rigorous modelling of the wavelength variation of the PSF FWHM including both more data points and potentially higher order terms is mandatory for future analysis, we decided to stick to this values in the present work, keeping in mind the large uncertainties which will affect the velocity dispersion maps in the modelling section. A representation of the FWHM variation with wavelength for 13 out of 16 observations is shown in Fig. 6. We have missing values of the FWHM for groups CGr34 (2 observations, 1 deep and 1 best-seeing) and CGr114. There appear to have a strong variations given the time of observation, up to 0.7 arcsec.

Having computed the PSF FWHM linear relation with wavelength for each FoV, we

are now able to derive the relevant value of the FWHM for galaxies at any redshift. Indeed, since all our observations are limited to the OII $\lambda 3727\,\text{Å}, 3729\,\text{Å}$ doublet, we can derive the wavelength of observation for each galaxy given its redshift with the usual relation

$$\lambda_{\text{obs}} = \lambda_{\text{em}}(1+z) \tag{10}$$

where z is the redshift or the galaxy and λ_{em}, λ_{obs} respectively the emitted (rest-frame) and observed wavelengths, and we can use this value to find the FWHM.

Considering that the FWHM is a measure of how spread a point-like source is in our images, and since we are interested in working with resolved enough galaxies in order to better constrain their kinematics, we would like galaxies to have a characteristic size at least above the FWHM. The only size which is given in the morphological catalogues is the half-light radius derived from optical images.

According to Swinbank et al. (2017) who compared the half-light radius of the nebular OII emission in MUSE images with that of their HST counterpart in ACS I or WFC H-band, the OII half-light radius seems to scale with the HST radius as

$$R_{1/2}^{\text{OII}} = (1.18 \pm 0.03) R_{1/2}^{\text{HST}} \tag{11}$$

Thus, choosing the FWHM as a lower limit for the morphological radius in our sample should get rid ourselves of most of unresolved galaxies without removing too many "good" galaxies. This is checked in the next sections.

2.4.2 SNR selection

The other information we can use to select our sample is the Signal to Noise Ratio (SNR), which tells us how well our galaxy is detached from the background. The SNR is generally derived as the ratio between the source's signal and the background level. The noisier an image, the lower the SNR is, which explains the need of a good data reduction pipeline.

As described in later sections, the galaxies must be automatically and then manually cleaned before fitting a kinematical model on the velocity maps in order to remove any noise dominated pixel which might compromise the fit. One of the criteria used by the routine to decide whether a pixel belongs to the galaxy or is noise-dominated is a lower limit on SNR (typically 5). Thus, if we want to have enough detection in our cleaned maps to perform the kinematical modelling, we must select galaxies with a strong enough SNR.

In our case, CAMEL[5] software, described in Epinat et al. (2012), was used on the integrated spectrum in order to derive spectral features of the galaxies. We used the OII flux and its error to derive the SNR as

[5] `https://bitbucket.org/bepinat/camel/src/master/`

$$\mathrm{SNR} = \frac{\text{OII flux}}{\text{OII flux error}} \tag{12}$$

This represents the OII SNR computed from the integrated galaxy spectrum using pixels within the smaller data cube centred around the galaxy. Since the typical SNR value used by the routine to clean the maps is around 5, we decided as a first step to choose an SNR lower limit of 10, allowing us to keep galaxies with strong enough detection after the automatic cleaning.

2.4.3 Selection criteria

To summarize, we decided to apply the two following cuts (lower limits):

- $R_{1/2,\mathrm{lim}} \approx \mathrm{FWHM} = 0.7\,\mathrm{arcsec}$
- $\mathrm{SNR}_{\mathrm{lim}} = 10$

It should be emphasized that these selection criteria should be used in combination rather than alone. Indeed, having a potentially large galaxy does not prevent us from having a low SNR per pixel, resulting in a too small cleaned galaxy for the kinematical modelling. In the same way, a high SNR could be obtained for a small galaxy, and we expect them to appear much larger in MUSE images because of beam smearing effects.

References

Bacon, R., Brinchmann, J., Richard, J., Contini, T., Drake, A., Franx, M., ... de Zeeuw, T. (2015, Mar). The MUSE 3D view of the Hubble Deep Field South. *Astronomy and Astrophysics*, *575*, A75. doi: 10.1051/0004-6361/201425419

Bacon, R., Conseil, S., Mary, D., Brinchmann, J., Shepherd, M., Akhlaghi, M., ... Carollo, M. (2017, Nov). The MUSE Hubble Ultra Deep Field Survey. I. Survey description, data reduction, and source detection. *Astronomy and Astrophysics*, *608*, A1. doi: 10.1051/0004-6361/201730833

Bertin, E., & Arnouts, S. (1996, June). SExtractor: Software for source extraction. *Astronomy and Astrophysics Supplement*, *117*, 393-404. doi: 10.1051/aas:1996164

Epinat, B., Tasca, L., Amram, P., Contini, T., Le Fèvre, O., Queyrel, J., ... Perret, V. (2012, Mar). MASSIV: Mass Assembly Survey with SINFONI in VVDS. II. Kinematics and close environment classification. *Astronomy and Astrophysics*, *539*, A92. doi: 10 .1051/0004-6361/201117711

Graham, A. W., Driver, S. P., Petrosian, V., Conselice, C. J., Bershady, M. A., Crawford, S. M., & Goto, T. (2005, Oct). Total Galaxy Magnitudes and Effective Radii from Petrosian Magnitudes and Radii. *The Astronomical Journal*, *130*(4), 1535-1544. doi: 10.1086/444475

Hubble, E. P. (1922, Oct). A general study of diffuse galactic nebulae. *Astrophysical Journal*, *56*, 162-199. doi: 10.1086/142698

Hubble, E. P. (1926, Dec). Extragalactic nebulae. *Astrophysical Journal*, *64*, 321-369. doi: 10.1086/143018

Laigle, C., McCracken, H. J., Ilbert, O., Hsieh, B. C., Davidzon, I., Capak, P., ... Zabl, J. (2016, June). THE COSMOS2015 CATALOG: EXPLORING THE $1 < z < 6$ UNIVERSE WITH HALF A MILLION GALAXIES. *The Astrophysical Journal Supplement Series*, *224*(2), 24. Retrieved 2019-03-21, from `http://stacks.iop.org/0067-0049/224/i=2/a=24?key=crossref.13400bd5b9499f45ce2b1d44c4a48475` doi: 10.3847/0067-0049/224/2/24

Moffat, A. F. J. (1969, December). A Theoretical Investigation of Focal Stellar Images in the Photographic Emulsion and Application to Photographic Photometry. *Astronomy and Astrophysics*, *3*, 455.

Peng, C. Y., Ho, L. C., Impey, C. D., & Rix, H.-W. (2002, July). Detailed Structural Decomposition of Galaxy Images. *The Astronomical Journal*, *124*, 266-293. doi: 10 .1086/340952

Sérsic, J. L. (1963). Influence of the atmospheric and instrumental dispersion on the brightness distribution in a galaxy. *Boletin de la Asociacion Argentina de Astronomia La Plata Argentina*, *6*, 41.

Simard, L. (1998, Jan). GIM2D: an IRAF package for the Quantitative Morphology Analysis of Distant Galaxies. In R. Albrecht, R. N. Hook, & H. A. Bushouse (Eds.), *Astronomical data analysis software and systems vii* (Vol. 145, p. 108).

Swinbank, A. M., Harrison, C. M., Trayford, J., Schaller, M., Smail, I., Schaye, J., ... Stott, J. P. (2017, May). Angular momentum evolution of galaxies over the past 10 Gyr: a MUSE and KMOS dynamical survey of 400 star-forming galaxies from z = 0.3 to 1.7. *Monthly Notices of the Royal Astronomical Society*, *467*(3), 3140-3159. doi: 10.1093/mnras/stx201

A Appendix

...